

Article

# Fe<sub>2</sub>O<sub>3</sub> nanoparticles decorated on graphene-carbon nanotubes conductive networks for boosting the energy density of all-solid-state asymmetric supercapacitor

Yadong Tian, Xin Hu, Yahui Wang, Chen Li, and Xiaoliang Wu

ACS Sustainable Chem. Eng., Just Accepted Manuscript • DOI: 10.1021/acsuschemeng.8b06857 • Publication Date (Web): 27 Apr 2019

Downloaded from <http://pubs.acs.org> on April 28, 2019

## Just Accepted

“Just Accepted” manuscripts have been peer-reviewed and accepted for publication. They are posted online prior to technical editing, formatting for publication and author proofing. The American Chemical Society provides “Just Accepted” as a service to the research community to expedite the dissemination of scientific material as soon as possible after acceptance. “Just Accepted” manuscripts appear in full in PDF format accompanied by an HTML abstract. “Just Accepted” manuscripts have been fully peer reviewed, but should not be considered the official version of record. They are citable by the Digital Object Identifier (DOI®). “Just Accepted” is an optional service offered to authors. Therefore, the “Just Accepted” Web site may not include all articles that will be published in the journal. After a manuscript is technically edited and formatted, it will be removed from the “Just Accepted” Web site and published as an ASAP article. Note that technical editing may introduce minor changes to the manuscript text and/or graphics which could affect content, and all legal disclaimers and ethical guidelines that apply to the journal pertain. ACS cannot be held responsible for errors or consequences arising from the use of information contained in these “Just Accepted” manuscripts.

Fe<sub>2</sub>O<sub>3</sub> nanoparticles decorated on graphene-carbon nanotubes conductive  
networks for boosting the energy density of all-solid-state asymmetric  
supercapacitor

Yadong Tian, Xin Hu, Yahui Wang, Chen Li, Xiaoliang Wu\*

\* Address correspondence to [wuxiaoliang90@163.com](mailto:wuxiaoliang90@163.com)

*Department of Chemistry and Chemical Engineering, College of Science, Northeast Forestry  
University, 26 Hexing Road, Harbin 150040, P. R. China*

ABSTRACT

Ferric oxide (Fe<sub>2</sub>O<sub>3</sub>) has drawn massive attentions as promising cathode electrode material for supercapacitor because of large theoretical specific capacity, low cost and abundance in nature. Nevertheless, its relatively low conductivity and large volume change seriously impede its electrochemical performance. Herein, Fe<sub>2</sub>O<sub>3</sub> nanoparticles decorated on graphene-carbon nanotubes (CNTs) conductive networks (Fe<sub>2</sub>O<sub>3</sub>/GNs/CNTs) were prepared by a simple reflux way. Owing to the unique structure, the Fe<sub>2</sub>O<sub>3</sub>/GNs/CNTs electrode delivers a notably enhanced specific capacity (675.7 F g<sup>-1</sup> at 1 A g<sup>-1</sup>) and superior rate characteristic in 6 M KOH aqueous electrolyte. More importantly, the as-constructed all-solid-state asymmetric device using Fe<sub>2</sub>O<sub>3</sub>/GNs/CNTs as cathode electrode and sulfurized CoAl layered double hydroxides (SLDH) as anode electrode shows the high energy density of 60.3 Wh kg<sup>-1</sup> and good electrochemical steadiness in KOH/PVA gel electrolyte. Therefore, this strategy provides a novel method to synthesize Fe<sub>2</sub>O<sub>3</sub> based electrode materials for energy storage system.

Keywords: Fe<sub>2</sub>O<sub>3</sub>; Graphene; CNTs; Energy density; Asymmetric supercapacitor

## Introduction

As resources wilt and environmental damage become more and more serious, it is imperative to develop environmentally friendly, efficient and inexpensive facilities for energy storage.<sup>1-3</sup> Among various energy storage facilities, supercapacitor has attracted tremendous interests owing to the inimitable features, for instance ultrahigh power density, ultrafast charge-discharge characteristic, superior electrochemical stabilization and environment friendly.<sup>4-7</sup> Nevertheless, most of supercapacitors are confronted with a relatively low energy density, which seriously restricts their widely utilization.<sup>8</sup> Therefore, it is urgent to enhance the energy density of supercapacitors to satisfy the increasing demand for high energy density facilities while maintaining their large power density. Based on the formula  $E = 1/2CV^2$ , the enhancement of energy density of supercapacitors can be obtained through improve the specific capacity (C) or/and enlarge the potential range (V).

Assembling asymmetric supercapacitors (ASCs) have been proved to be an efficacious way to enlarge the device voltage range by combination of voltage range of cathode and anode electrodes, resulting in a remarkable improvement of energy density<sup>9-12</sup> Up to now, a significant advancement has been made to develop anode electrodes for ASCs, for example  $\text{MnO}_2$ ,  $\text{Co}_3\text{O}_4$ ,  $\text{Ni(OH)}_2$ ,  $\text{NiCoS}_4$ , etc.<sup>13-18</sup> Porous carbon with double layer charge storage mechanism are usually used as cathode electrodes, which usually suffer from low specific capacity. Consequently, the energy density of ASCs is badly limited by the poor specific capacity of cathode electrodes. As a kind of cathode electrode material, ferric oxide ( $\text{Fe}_2\text{O}_3$ ) materials have received extensive attentions because of the large theoretical specific capacity, low cost and abundance in nature.<sup>19-24</sup> Especially, iron element owns various oxidation states, which can generate reversible redox reaction within the cathode voltage regions. Such as, Shivakumara synthesized porous flower-like  $\alpha\text{-Fe}_2\text{O}_3$  material through the self-assembly strategy and the prepared electrode delivers a capacitance of  $127 \text{ F g}^{-1}$  at  $1 \text{ A g}^{-1}$ .<sup>25</sup> Zheng

prepared hollow nanoshuttle-like  $\alpha$ -Fe<sub>2</sub>O<sub>3</sub> through a convenient hydrothermal way and the obtained materials deliver a large capacity of 249 F g<sup>-1</sup> at 0.5 A g<sup>-1</sup>.<sup>26</sup> Although, great achievements have been achieved, the electrochemical properties of Fe<sub>2</sub>O<sub>3</sub> are not satisfied with actual applications because of the low conductivity and large volume change. Currently, combining with conductive materials to construct composite is an efficacious method to improve the conductivity and capacitive property of Fe<sub>2</sub>O<sub>3</sub>-based materials.<sup>20</sup> Nano-structured carbon materials for instance CNTs and graphene are regard as the excellent conductive substrate for construction of composites because of the good conductivity and high specific surface area.<sup>27, 28</sup> Especially, the unique structure of graphene can effectively impede the agglomeration and reduce the size of nanoparticles, generating more electroactive sites.<sup>29</sup> Moreover, in contrast to single graphene that enhances merely one aspect of performances, graphene-CNTs conductive networks can improve overall property of the electrode due to the synergetic effect.<sup>30</sup> Hence, the development of new nano-structured carbon material/Fe<sub>2</sub>O<sub>3</sub> is favorable for achieving high performance supercapacitor.

Herein, we develop a convenient route to prepare Fe<sub>2</sub>O<sub>3</sub>/graphene nanosheets/CNTs (Fe<sub>2</sub>O<sub>3</sub>/GNs/CNTs) composite as electrode materials for supercapacitor. Due to the unique electrical and structural support, the Fe<sub>2</sub>O<sub>3</sub>/GNs/CNTs electrode delivers large specific capacity and superior rate characteristic in 6 M KOH solution. More importantly, the as-constructed asymmetric device using Fe<sub>2</sub>O<sub>3</sub>/GNs/CNTs as cathode electrode and sulfurized CoAl layered double hydroxides (SLDH) as anode electrode exhibits high energy density and superior electrochemical steadiness in KOH/PVA gel electrolyte.

## Results and discussion

### *Characterization of cathode electrode material*

The microstructures of the prepared materials were checked by scanning/transmission electron microscopy (SEM/TEM). As seen in Fig. 1a, pure Fe<sub>2</sub>O<sub>3</sub> materials display a

1  
2  
3 block-like structure with the size of 20-50 nm. For  $\text{Fe}_2\text{O}_3/\text{GNs}$  composite, the  $\text{Fe}_2\text{O}_3$   
4 nanoparticles are wrapped by graphene nanosheets (Fig. S1a), the unique structure can  
5 effectively prevent the aggregating of  $\text{Fe}_2\text{O}_3$  and enhanced conductive property of the  
6 composite. After the introduction of carbon nanotubes to form a porous but secure structure  
7 (Fig. 1b), which can offer barrier-free access for electrolyte ions fast diffusion during  
8 charge/discharge procedure. The element mapping images of  $\text{Fe}_2\text{O}_3/\text{GNs}/\text{CNTs}$  exhibit the  
9 homogeneous distribution of O, Fe and C elements (Fig. S1c-e). Furthermore, TEM image  
10 further confirms the  $\text{Fe}_2\text{O}_3$  nanoparticles randomly distribute and closely anchor on the  
11 surface of graphene-CNTs conductive networks (Fig. 1c), which facilitating electrons fast  
12 transport during the charge/discharge procedure. Remarkably, from the high-resolution TEM  
13 observed, the morphology of  $\text{Fe}_2\text{O}_3$  transforms into ultra-small nanoparticles ( $<10$  nm, Fig. 1d  
14 mark with blue circles) after the introduction of GNs because of more iron ion nucleation sites  
15 supplied by GNs.<sup>29</sup>

16  
17  
18  
19  
20  
21  
22  
23  
24  
25  
26  
27  
28  
29  
30  
31  
32  
33 The crystal structure characteristic of the prepared materials was performed by X-ray  
34 diffraction (XRD). As seen in Fig. 2a, the diffraction peaks of  $\text{Fe}_2\text{O}_3$  and  $\text{Fe}_2\text{O}_3/\text{GNs}/\text{CNTs}$  at  
35 about  $2\theta = 24.0^\circ, 33.1^\circ, 35.5^\circ, 40.7^\circ, 49.4^\circ, 54.0^\circ, 62.5^\circ$  and  $63.9^\circ$  can be ascribed to the (012),  
36 (104), (110), (113), (024), (116), (214) and (300) planes of  $\text{Fe}_2\text{O}_3$  (PDF#33-0664),  
37 respectively. Furthermore, compared with the pure  $\text{Fe}_2\text{O}_3$ , the characteristic peaks of  
38  $\text{Fe}_2\text{O}_3/\text{GNs}/\text{CNTs}$  became weaker due to the  $\text{Fe}_2\text{O}_3$  nanoparticles were wrapped by GNs. The  
39 peak at  $25^\circ$  represent the (002) plane of GNs cannot be seen for  $\text{Fe}_2\text{O}_3/\text{GNs}/\text{CNTs}$  due to the  
40 surface of graphene-CNTs conductive networks was covered with nanosized  $\text{Fe}_2\text{O}_3$ , and this  
41 phenomenon can be found in the reported literature.<sup>23, 30</sup> Raman spectra of the pure  $\text{Fe}_2\text{O}_3$  and  
42  $\text{Fe}_2\text{O}_3/\text{GNs}/\text{CNTs}$  composite are displayed in Fig. 2b. The diffraction peaks at 214, 288, 403  
43 and  $602\text{ cm}^{-1}$  can be found in  $\text{Fe}_2\text{O}_3$  and  $\text{Fe}_2\text{O}_3/\text{GNs}/\text{CNTs}$ , which are in good agreement with  
44 reported results of  $\text{Fe}_2\text{O}_3$ .<sup>23</sup> In addition, the ratio of D peak to G peak of  $\text{Fe}_2\text{O}_3/\text{GNs}/\text{CNTs}$  is  
45  
46  
47  
48  
49  
50  
51  
52  
53  
54  
55  
56  
57  
58  
59  
60

0.98, demonstrating partly functional groups remain after reflux. Fig. 2c displays the Fourier transform infrared (FT-IR) spectrums of graphene oxide (GO) and Fe<sub>2</sub>O<sub>3</sub>/GNs/CNTs. The absorption bands located at 1643 and 1380 are corresponding to C=O and C-O in COOH, at 1320 and 1110 cm<sup>-1</sup> are corresponding to the C-OH stretching vibration, C-O stretching vibration in C-O-C. After reflux, the strength of these peaks for the oxygen functional groups is distinctly weakened, further suggesting the partial removal of oxygen functional groups.

The chemical constitution and bonding states of the Fe<sub>2</sub>O<sub>3</sub>/GNs/CNTs materials were detected through X-ray photoelectron spectroscopy (XPS). The XPS measurement spectrum of Fe<sub>2</sub>O<sub>3</sub>/GNs/CNTs confirms that the composite is consisting of C, O, and Fe elements (Fig. 2d). The C 1s spectrum (Fig. S2a) can be divided into four peaks that ascribed to C=C (284.5 eV), C-C (285.0 eV), C-O (286.7 eV), and C=O (288.6 eV) bonds, respectively, suggesting conductive carbon substrate containing moderate oxygen functional groups. From the Fe 2p spectrum (Fig. 2e), two main peaks are situated at 707.4 and 720.1 eV attributed to Fe 2p<sub>3/2</sub> and Fe 2p<sub>1/2</sub>, which in good accordance with the previously reported Fe<sub>2</sub>O<sub>3</sub> materials in literature.<sup>24</sup> The specific surface area of the Fe<sub>2</sub>O<sub>3</sub>/GNs/CNTs samples were tested through nitrogen adsorption/desorption isotherms (Fig. S2). The Fe<sub>2</sub>O<sub>3</sub>/GNs/CNTs samples show a large specific surface area of 220 m<sup>2</sup> g<sup>-1</sup>, larger than the published results in literatures.<sup>27, 28</sup> The mass-loading of Fe<sub>2</sub>O<sub>3</sub> in the Fe<sub>2</sub>O<sub>3</sub>/GNs/CNTs composites was determined by thermal gravimetric analysis (TGA) in air. As seen in Fig. 2f, the mass-loading of Fe<sub>2</sub>O<sub>3</sub> in the Fe<sub>2</sub>O<sub>3</sub>/GNs/CNTs samples is about 55.5 wt.%.

The electrochemical characteristics of the Fe<sub>2</sub>O<sub>3</sub>/GNs/CNTs samples were firstly measured by cyclic voltammetry (CV) in aqueous solutions of 6 M KOH electrolyte. As seen in Fig. 3a, all the CV profiles of the Fe<sub>2</sub>O<sub>3</sub>/GNs/CNTs electrode show one pair of strong redox peaks, demonstrating that the specific capacity are primarily come from Faradaic redox reactions. The strong redox peaks are ascribed to the reversible transition of Fe<sup>2+</sup> and Fe<sup>3+</sup>.

Remarkably, as the scan rates increasing, the contour of CV profiles shows no apparent distortion, indicating fast charge transfer kinetics and superior rate performance. Galvanostatic charge-discharge (GCD) was tested to assess the electrochemical behavior of the  $\text{Fe}_2\text{O}_3/\text{GNs}/\text{CNTs}$  materials. The GCD profiles of the  $\text{Fe}_2\text{O}_3$ ,  $\text{Fe}_2\text{O}_3/\text{GNs}$  and  $\text{Fe}_2\text{O}_3/\text{GNs}/\text{CNTs}$  electrodes show obvious Faraday pseudocapacity characteristic with a discharge platform occur at around -0.9 V (Fig. 3b). The  $\text{Fe}_2\text{O}_3/\text{GNs}/\text{CNTs}$  electrode delivers a longer discharge time than other electrodes, suggesting a higher specific capacitance for  $\text{Fe}_2\text{O}_3/\text{GNs}/\text{CNTs}$ . The specific capacities of the  $\text{Fe}_2\text{O}_3/\text{GNs}/\text{CNTs}$  electrodes were calculated and displayed in Fig. 3d based on the discharge curves (Fig. 3c). The  $\text{Fe}_2\text{O}_3/\text{GNs}/\text{CNTs}$  electrode delivers a high specific capacitance of  $675.7 \text{ F g}^{-1}$  at  $1 \text{ A g}^{-1}$  based on the electroactive material, which is comparable with those of  $\text{Fe}_2\text{O}_3$  ( $322.6 \text{ F g}^{-1}$ ),  $\text{Fe}_2\text{O}_3/\text{GNs}$  ( $606.5 \text{ F g}^{-1}$ ) and other formerly published Fe-based electrodes in literatures (Table 1). Remarkably, even the  $\text{Fe}_2\text{O}_3/\text{GNs}/\text{CNTs}$  electrode retains  $345.4 \text{ F g}^{-1}$  at  $50 \text{ A g}^{-1}$ , meaning superior rate characteristic. Electrochemical impedance was further investigated the electrode kinetics of the obtained samples. As seen in Fig. 3e, the ohmic resistance of the electrolyte and cell components ( $R(\text{e})$ ) of the  $\text{Fe}_2\text{O}_3/\text{GNs}/\text{CNTs}$  electrode ( $0.31 \Omega$ ) is lower than  $\text{Fe}_2\text{O}_3/\text{GNs}$  ( $0.39 \Omega$ ) and  $\text{Fe}_2\text{O}_3$  ( $0.59 \Omega$ ), indicating a much better conductivity for  $\text{Fe}_2\text{O}_3/\text{GNs}/\text{CNTs}$ . Moreover, the combination of surface and charge-transfer resistance  $R(\text{s+ct})$  of the  $\text{Fe}_2\text{O}_3/\text{GNs}/\text{CNTs}$  electrode is much lower than  $\text{Fe}_2\text{O}_3$  and  $\text{Fe}_2\text{O}_3/\text{GNs}$ , confirming a rapider charge-transfer rate for  $\text{Fe}_2\text{O}_3/\text{GNs}/\text{CNTs}$ . Cycling life of the  $\text{Fe}_2\text{O}_3/\text{GNs}/\text{CNTs}$  electrode was measured at  $5 \text{ A g}^{-1}$  for 5000 cycles. As displayed in Fig. 3f, after 5,000 cycle tests, the  $\text{Fe}_2\text{O}_3/\text{GNs}/\text{CNTs}$  electrode can keep 82.4% of the original capacity, indicating superior cycling steadiness. Notably, after cycling process, the  $\text{Fe}_2\text{O}_3/\text{GNs}/\text{CNTs}$  samples can still maintain the original stable structure with almost no deformation.

The Fe<sub>2</sub>O<sub>3</sub>/GNs/CNTs composite shows good electrochemical properties because of the unique structure. (1) The large specific surface area of Fe<sub>2</sub>O<sub>3</sub>/GNs/CNTs can supply massive reactive sites to the sufficient utilize the pseudocapacitive characteristics of Fe<sub>2</sub>O<sub>3</sub>. (2) Fe<sub>2</sub>O<sub>3</sub> nanoparticles are wrapped by graphene nanosheets with CNTs-bridged frameworks to form a porous but secure structure, which can not only offer barrier-free access for electrolyte ions fast transport during charge/discharge procedure, but also effectively buffer volume change of Fe<sub>2</sub>O<sub>3</sub>/GNs/CNTs during charge/discharge procedure to ensure good electrochemical stability. (3) The outstanding conductivity of graphene and CNTs can construct a fast conductive network for electrons rapid transport along overall of the electrode materials.

#### *Characterization of anode electrode materials*

The morphology and microstructure of the CoAl layered double hydroxides (LDH) and SLDH samples were checked by SEM and TEM. As seen in Fig. 4a, the SEM image of LDH materials show a lamellar structure and agglomerated together. After sulfurization, the SLDH samples (Fig. 4b) still retaining lamellar structure with part of fragmentation. Furthermore, the TEM image of LDH materials (Fig. 4c) confirms the lamellar structure with the lateral dimension in the scope of 30-60 nm. After sulfurization, the SLDH samples (Fig. 4d) display an amorphous lamellar porous structure, which can not only generate more redox active sites but also facilitate the ions rapid diffusion. The crystal structures of the LDH and SLDH samples were checked by XRD measurements. The XRD pattern (Fig. 5a) of the LDH samples is in accord with CoAl-LDH (JCPDS No. 51-0045). Nevertheless, no distinct characteristic peaks can be detected in the XRD pattern of SLDH, suggesting an amorphous structure after the sulfurization, which is in agreement with the published result in literature.<sup>43</sup> The absence of long-range crystalline order in the process of sulfur substituted hydroxide and, therefore, the amorphous structure. The chemical constitution and bonding states of the SLDH material was checked through X-ray photoelectron spectroscopy (XPS). As seen in Fig. 5b,



the XPS survey spectrum of SLDH reveals the composite consists of Co, Al, O, and S elements. The Co 2p spectrum (Fig. 5c) was spin-orbit split into two major peaks situated at 781.2 eV and 797.1 eV with satellites accordingly, which are composed of Co 2p<sub>1/2</sub> and Co 2p<sub>3/2</sub> components, demonstrating the existence of Co<sup>2+</sup> and Co<sup>3+</sup> in SLDH samples. For S 2p spectrum (Fig. 5d), the peaks around at 163.2 and 162.0 eV were attributed to S 2p<sub>1/2</sub> and S 2p<sub>3/2</sub> of metal–sulfur bonds. The peak at 74.2 eV was attributed to Al 2p (Fig. S3a), confirming the present of Al<sup>3+</sup> in the composite. The nitrogen adsorption/desorption isotherms of SLDH (Fig. S3b) shows a typical IV isotherm with a high specific surface area of 58 m<sup>2</sup> g<sup>-1</sup> due to the porous structure after sulfurization.

The electrochemical capabilities of the SLDH samples were measured by CV and GCD tests in 6 M KOH solution. The CV profiles of the LDH and SLDH electrode show one pair of obvious redox peaks at 10 mV s<sup>-1</sup> (Fig. 6a), suggesting the Faradaic pseudocapacitive characteristics of the LDH and SLDH electrodes. Furthermore, it can be clearly observed that the redox peak shifts to the cathode range after sulfur substitution. The possible Faraday redox reaction for SLDH electrode could be expressed by the following expression:



The CV curve of the SLDH electrode shows a relative bigger integrated area than that of LDH electrode, demonstrating a higher specific capacity for SLDH. The increased specific capacity is due to the amorphous porous lamellar structure after sulfurization, which can supply more redox active sites and facilitate ion fast diffusion during charge-discharge procedure. As displayed in Fig. 6b, even at large scan rates, the CV profile of SLDH electrode were well-maintained, indicating fast charge transfer kinetics and good rate characteristic. Moreover, accord with CV results, the GCD profiles of the SLDH electrode shows typical pseudocapacitive characteristics (Fig. 6c). The GCD profile of the SLDH electrode show no

distinct IR drop at  $10 \text{ A g}^{-1}$ , suggesting small internal resistance. The specific capacities were computed according to the GCD profiles and shown in Fig. 6d. The SLDH electrode displays a superior specific capacitance of  $1005.1 \text{ F g}^{-1}$  at  $0.5 \text{ A g}^{-1}$  according to the electroactive materials, much higher than that of LDH. Significantly, the SLDH electrode shows a good rate performance of 74.3 % at  $20 \text{ A g}^{-1}$ , much better than that of LDH and previously reported LDH and metal sulfide in literatures (Table S1). The good rate performance is due to the amorphous porous structure after sulfurization, which is in favor of the rapid diffusion of ions. To explore the electrode kinetics, electrochemical impedance spectroscopy was tested and shown in Fig. 6e. The  $R(e)$  of the SLDH electrode is  $0.32 \Omega$ , which is lower than that of LDH ( $0.36 \Omega$ ), indicating a much better conductivity for SLDH. Additionally, in the low-frequency scope, the SLDH electrode displays an almost vertical line, meaning a fast electron transfer rate. Cycling life of the SLDH electrode was measured at  $5 \text{ A g}^{-1}$  and displayed in Fig. 6f. The SLDH electrode can keep 88.7% of the original capacity after 5,000 cycles, confirming superior cycling steadiness. Notably, after cycling process, the SLDH samples can still maintain the original lamellar structure with almost no deformation.

#### *Characterizations of asymmetric supercapacitor*

To further assess the electrochemical characteristics of the obtained samples, all-solid-state ASC equipment was assembled using the  $\text{Fe}_2\text{O}_3/\text{GNs}/\text{CNTs}$  material as the cathode electrode and the SLDH material as the anode electrode in PVA/KOH gel electrolyte. Fig. 7a shows a steady potential region range from -1.1 to 0 V for  $\text{Fe}_2\text{O}_3/\text{GNs}/\text{CNTs}$  electrode and from 0.0 to 0.4 V for SLDH electrode in a three-electrode system. The quality ratio of the anode electrode to cathode electrode was computed based on the formula (3). The CV profiles of the optimized  $\text{Fe}_2\text{O}_3/\text{GNs}/\text{CNTs}/\text{SLDH}$  ASC were measured at  $10 \text{ mV s}^{-1}$  in different potential region in PVA/KOH gel electrolyte. As seen in Fig. S4a, no distinct increase of anodic current can be seen even at 1.6 V, indicating a wide potential region of 0-1.6 V can be

steadily obtained. The wide voltage range is conducive to achieving a larger energy density, hence the electrochemical property of the ASC were tested from 0 to 1.6 V. Fig. S4b displays the CV profiles of the optimized ASC measured at various scan rates in the voltage range of 0-1.6 V. The contour of the CV profiles demonstrates that the capacity originates from the combination of both pseudocapacity and electric double-layer capacity. The GCD profiles of the ASC shows typical pseudocapacitive characteristics (Fig. 7b). The all-solid-state ASC has a large specific capacity of  $169.5 \text{ F g}^{-1}$  at  $0.5 \text{ A g}^{-1}$ . Benefiting from its wide voltage range and high specific capacity, the optimized ASC achieves a high energy density of  $60.3 \text{ Wh kg}^{-1}$  (Fig. 7c), which is better than these of previous published Fe-based ASC devices, such as,  $\text{Fe}_2\text{O}_3/\text{CNT}/\text{MnO}_2/\text{CNT}$  ( $45.8 \text{ Wh kg}^{-1}$ ),<sup>43</sup>  $\text{Fe}_3\text{O}_4/\text{Co}_2\text{AlO}_4@\text{MnO}_2$  ( $35.25 \text{ Wh kg}^{-1}$ ),<sup>44</sup>  $\text{Fe}_2\text{O}_3/\text{V}_2\text{O}_5$  ( $32.2 \text{ Wh kg}^{-1}$ ),<sup>45</sup>  $\text{Fe}_3\text{O}_4@\text{Fe}_2\text{O}_3/\text{Fe}_3\text{O}_4@\text{MnO}_2$  ( $26.6 \text{ Wh kg}^{-1}$ ),<sup>46</sup>  $\text{Fe}_2\text{O}_3/\text{NiO}$  ( $12.4 \text{ Wh kg}^{-1}$ ).<sup>47</sup> Fig. S4c displays the CV profiles of the assembled ASC at different bent angles. In addition, the  $\text{Fe}_2\text{O}_3/\text{GNs}/\text{CNTs}/\text{SLDH}$  ASC can maintain an initial specific capacity of 82.2% after cyclic tests of 5000 cycles at  $5 \text{ A g}^{-1}$  (Fig. 7d), demonstrating good electrochemical stability. More interestingly, two series connected  $\text{Fe}_2\text{O}_3/\text{GNs}/\text{CNTs}/\text{SLDH}$  ASC devices can light the red commercial light emitting diodes (LEDs) for 30 min and run a small fan, demonstrating its practical application (inset of Fig. 7d).

## Conclusions

In summary, we develop a convenient, one-step route to prepare  $\text{Fe}_2\text{O}_3$ /graphene nanosheets/CNTs ( $\text{Fe}_2\text{O}_3/\text{GNs}/\text{CNTs}$ ) composite as electrode materials for supercapacitor. Benefiting from the unique structure, the  $\text{Fe}_2\text{O}_3/\text{GNs}/\text{CNTs}$  electrode delivers superior specific capacity and superior rate characteristic in 6 M KOH solution. More importantly, the as-constructed all-solid-state ASC using  $\text{Fe}_2\text{O}_3/\text{GNs}/\text{CNTs}$  as cathode electrode and SLDH as anode electrode shows high energy density and excellent electrochemical steadiness in KOH/PVA gel electrolyte.

## ASSOCIATED CONTENT

Supporting Information is available free of charge on the ACS Publications website at xxx

Experimental Section, SEM image, elemental mapping images, XPS spectra, Nitrogen adsorption-desorption isotherms, CV curves and specific capacitance at different scan rates. (PDF)

## AUTHOR INFORMATION

### Corresponding Author

Email:wuxiaoliang90@163.com

### ORCID

Xiaoliang Wu: 0000-0002-9297-0922

### Notes

The authors declare no competing financial interest

## ACKNOWLEDGMENTS

This work was supported by National Natural Science Foundation of China (51702043) and Heilongjiang Postdoctoral Foundation (LBH-Z18008).

## REFERENCES

- [1] Guan, B.; Yu, X.; Wu, H.; Lou, X. Complex nanostructures from materials based on metal–organic frameworks for electrochemical energy storage and conversion, *Adv. Mater.* **2017**, 29, 1703614, DOI 10.1002/adma.201703614.
- [2] Wang, Q.; Yan, J.; Fan, Z.; Carbon materials for high volumetric performance supercapacitors: design, progress, challenges and opportunities, *Energy Environ. Sci.* **2016**, 9, 729-762, DOI 10.1039/c5ee03109e.
- [3] Zardkhoshoui, A. M.; Davarani, S. S. H. Flexible asymmetric supercapacitors based on CuO@MnO<sub>2</sub>-rGO and MoS<sub>2</sub>-rGO with ultrahigh energy density, *J. Electroanal. Chem.* **2018**, 827, 221–229, DOI 10.1016/j.jelechem.2018.08.023.
- [4] Ling, Z.; Wang, Z.Y.; Zhang, M.D.; Yu, C.; Wang, G.; Dong, Y.F.; Liu, S.H.; Wang, Y.W.; Qiu, J.S. Sustainable synthesis and assembly of biomass-derived B/N co-doped carbon nanosheets with ultrahigh aspect ratio for high-performance supercapacitors, *Adv. Funct. Mater.* **2016**, 26, 111–119, DOI 10.1002/adfm.201504004.
- [5] Ding, B.; Guo, D.; Wang, Y.H.; Wu, X.L.; Fan, Z.J. Functionalized graphene nanosheets decorated on carbon nanotubes networks for high performance supercapacitors. *J. Power Sources* **2018**, 398, 113–119, DOI.org/10.1016/j.jpowsour.2018.07.063.
- [6] Guo, D.; Ding, B.; Hu, X.; Wang, Y.; Han, F.; Wu, X. Synthesis of boron and nitrogen codoped porous carbon foam for high performance supercapacitors, *ACS Sustainable Chem. Eng.* **2018**, 6, 11441-11449, DOI 10.1021/acssuschemeng.8b01435.
- [7] Zardkhoshoui, A. M.; Davarani, S. S. H. Synthesis of NiGa<sub>2</sub>S<sub>4</sub>-rGO on nickel foam as advanced electrode for flexible solid-state supercapacitor with superior energy density. *J. Colloid. Interf. Sci.* **2019**, 535, 195-204, DOI 10.1016/j.jcis.2018.09.100.
- [8] Wu, X.; Jiang, L.; Long, C.; Wei, T.; Fan, Z.; Dual support system ensuring porous Co–Al hydroxide nanosheets with ultrahigh rate performance and high energy density for

- supercapacitors, *Adv. Funct. Mater.* **2015**, 25, 1648-1655, DOI 10.1002/adfm.201404142.
- [9] Yang, J.; Yu, C.; Fan, X.M.; Liang, S.X.; Li, S.F.; Huang, H.W. Ling, Z.; Hao, C.; Qiu, J.S. Electroactive edge site-enriched nickel-cobalt sulfide into graphene frameworks for high-performance asymmetric supercapacitors, *Energy Environ. Sci.* **2016**, 9, 1299-1307, DOI 10.1039/c5ee03633j.
- [10] Lei, Z.; Zhang, J.; Zhao, X. Ultrathin MnO<sub>2</sub> nanofibers grown on graphitic carbonspheres as high-performance asymmetric supercapacitor electrodes, *J. Mater. Chem.* **2012**, 22, 153-160, DOI 10.1039/c1jm13872c.
- [11] Yan, J.; Fan, Z.; Sun, W.; Ning, G.; Wei, T.; Zhang, Q.; Zhang, R.; Zhi, L.; Wei, F. Advanced asymmetric supercapacitors based on Ni(OH)<sub>2</sub>/graphene and porous graphene electrodes with high energy density, *Adv. Funct. Mater.* **2012**, 22, 2632-2641, DOI 10.1002/adfm.201102839.
- [12] Zardkhoshoui, A. M.; Davarani, S. S. H.; Hashemi, Masumeh. Fabrication of cobalt gallium oxide with zinc iron oxide on nickel foam for a high-performance asymmetric supercapacitor, *New J. Chem.* **2019**, 43, 4590-4598, DOI 10.1039/c8nj05854g.
- [13] Chang, J.; Jin, M.; Yao, F.; Kim, T.; Le, V.; Yue, H.; Gunes, F.; Li, B.; Ghosh, A.; Xie, S.; Lee, Y. Asymmetric supercapacitors based on graphene/MnO<sub>2</sub> nanospheres and graphene/MoO<sub>3</sub> nanosheets with high energy density, *Adv. Funct. Mater.* **2013**, 23, 5074-5083, DOI 10.1002/adfm201301851.
- [14] Xu, J.; Wang, Q.F.; Wang, X.M.; Xiang, Q.Y.; Liang, B.; Chen, D.; Shen, G.Z. Flexible asymmetric supercapacitors based on Co<sub>9</sub>S<sub>8</sub> nanorod//Co<sub>3</sub>O<sub>4</sub>@RuO<sub>2</sub> nanosheet arrays on carbon cloth, *ACS Nano*. **2013**, 7, 5453-5462, DOI 10.1021/nn401450s.
- [15] Zardkhoshoui, A. M.; Davarani, S. S. H. Ultrahigh energy density supercapacitors based on facile synthesized Ni,CoOH-rGO/NF hybrid electrodes, *J. Alloy. Compd.* **2018**, 769, 922-931, DOI 10.1016/j.jallcom.2018.07.321.

- [16] Yang, J.; Yu, C.; Fan, X.; Qiu, J. 3D architecture materials made of NiCoAl-LDH nanoplates coupled with NiCo-carbonate hydroxide nanowires grown on flexible graphite paper for asymmetric supercapacitors, *Adv. Energy Mater.* **2014**, 4, 1400761, DOI 10.1002/aenm.201400761.
- [17] Zardkhoshoui, A. M.; Davarani, S. S. H. All-solid-state, flexible, ultrahigh performance supercapacitors based on the Ni-Al LDH-rGO electrodes. *J. Alloy. Compd.* **2018**, 750, 515-522, DOI 10.1016/j.jallcom.2018.04.027.
- [18] Li, Y.H.; Cao, L.J.; Qiao, L.; Zhou, M.; Yang, Y.; Xiao, P.; Zhang, Y.H. Ni-Co sulfide nanowires on nickel foam with ultrahigh capacity for asymmetric supercapacitors, *J. Mater. Chem. A* **2014**, 2, 6540-6548, DOI 10.1039/c3ta15373h.
- [19] Zeng, Y.X.; Yu, M.H.; Meng, Y.; Fang, P.P.; Lu, X.H.; Tong, Y.X. Iron-based supercapacitor electrodes: advances and challenges, *Adv. Energy Mater.* **2016**, 6, 1601053, DOI 10.1002/aenm.201601053.
- [20] Nithya, V.D.; Arul, N.S. Review on  $\alpha$ -Fe<sub>2</sub>O<sub>3</sub> based cathode electrode for high performance supercapacitors, *J. Power Sources* **2016**, 327, 297-318, DOI 10.1016/j.jpowsour.2016.07.033.
- [21] Zardkhoshoui, A. M.; Davarani, S. S. H. Designing a flexible all-solid-state supercapacitor based on CuGa<sub>2</sub>O<sub>4</sub> and FeP-rGO electrodes. *J. Alloys Compd* **2018**, 773, 527-536, DOI 10.1016/j.jallcom.2018.09.135.
- [22] Liang, H.; Xia, C.; Emwas, A.; Anjum, D.; Miao, X.; Alshareef, H. Phosphine plasma activation of  $\alpha$ -Fe<sub>2</sub>O<sub>3</sub> for high energy asymmetric supercapacitors, *Nano Energy* **2018**, 49, 155-162, DOI 10.1016/j.nanoen.2018.04.032.
- [23] Wang, Y.; Zhang, M.; Pan, D.; Li, Y.; Ma, T. Xie, J. Nitrogen/sulfur co-doped graphene networks uniformly coupled N-Fe<sub>2</sub>O<sub>3</sub> nanoparticles achieving enhanced supercapacitor performance, *Electrochim. Acta* **2018**, 266, 242-253, DOI 10.1016/j.electacta.2018.

02.040.

- [24] Chen, J.; Xu, J.; Zhou, S.; Zhao, N.; Wong, C. Template-grown graphene/porous Fe<sub>2</sub>O<sub>3</sub> nanocomposite: A high-performance anode material for pseudocapacitors, *Nano Energy* **2015**, 15, 719-728, DOI 10.1016/j.nanoen.2015.05.021.
- [25] Shivakumara, S.; Penki, T.R.; Munichandraiah, N. Synthesis and characterization of porous flowerlike  $\alpha$ -Fe<sub>2</sub>O<sub>3</sub> nanostructures for supercapacitor application, *ECS Electrochem. Lett.* **2013**, 2, 60-62, DOI 10.1149/2.002307eel.
- [26] Zheng, X.; Yan, X.Q.; Sun, Y.H.; Yu, Y.S.; Zhang, G.J.; Shen, Y.W.; Liang, Q.J.; Liao, Q.L.; Zhang, Y. Temperature-dependent electrochemical capacitive performance of the  $\alpha$ -Fe<sub>2</sub>O<sub>3</sub> hollow nanoshuttles as supercapacitor electrodes, *J. Colloid. Interf. Sci.* **2016**, 466, 291-296, DOI 10.1016/j.jcis.2015.12.024.
- [27] Ma, Z.; Huang, X.; Dou, S.; Wu, J.; Wang, S. One-pot synthesis of Fe<sub>2</sub>O<sub>3</sub> nanoparticles on nitrogen-doped graphene as advanced supercapacitor electrode materials, *J. Phys. Chem. C* **2014**, 118, 17231-17239, DOI 10.1021/jp502226j.
- [28] Wang, H.; Xu, Z.; Yi, H.; Wei, H.; Guo, Z.; Wang, X. One-step preparation of single-crystalline Fe<sub>2</sub>O<sub>3</sub> particles/graphene composite hydrogels as high performance anode materials for supercapacitors, *Nano Energy*. **2014**, 7, 86-96, DOI 10.1016/j.nanoen.2014.04.009.
- [29] Yan, J.; Fan, Z.; Sun, W.; Ning, G.; Wei, T.; Zhang, Q.; Zhang, R.; Zhi, L.; Wei, F. Advanced asymmetric supercapacitors based on Ni(OH)<sub>2</sub>/graphene and porous graphene electrodes with high energy density, *Adv. Funct. Mater.* **2012**, 22, 2632-2641, DOI 10.1002/adfm.201102839.
- [30] Long, C.; Jiang, L.; Wei, T.; Yan, J.; Fan, Z. High-performance asymmetric supercapacitors with lithium intercalation reaction using metal oxide-based composites as electrode materials, *J. Mater. Chem. A* **2014**, 2, 16678-16686, DOI



- 10.1039/c4ta03241a.
- [31] Tang, Q.; Wang, W.; Wang, G. The perfect matching between the low-cost Fe<sub>2</sub>O<sub>3</sub> nanowire anode and the NiO nanoflake cathode significantly enhances the energy density of asymmetric supercapacitors, *J. Mater. Chem. A* **2015**, 3, 6662-6670, DOI 10.1039/c5ta00328h.
- [32] Zhang, M.; Chen, K.; Chen, X.; Peng, X.; Sun, X.; Xue, D. Ethylenediamine-assisted crystallization of Fe<sub>2</sub>O<sub>3</sub> microspindles with controllable size and their pseudocapacity performance, *CrystEngComm*. **2015**, 17, 1521-1525, DOI 10.1039/c4ce02417f.
- [33] Yang, P.; Ding, Y.; Lin, Z.; Chen, Z.; Li, Y.; Qiang, P.; Ebrahimi, M.; Mai, W.; Wong, C.; Wang, Z. Low-cost high-performance solid-state asymmetric supercapacitors based on MnO<sub>2</sub> nanowires and Fe<sub>2</sub>O<sub>3</sub> nanotubes, *Nano Lett.* **2014**, 14, 731-736, DOI 10.1021/nl404008e.
- [34] Wang, D.; Wang, Q.; Wang, T. Controlled synthesis of mesoporous hematite nanostructures and their application as electrochemical capacitor electrodes, *Nanotechnology* **2011**, 22, 135604, DOI 10.1088/0957-4484/22/13/135604 .
- [35] Nasibi, M.; Golozar, M.; Rashed, G. Nano iron oxide (Fe<sub>2</sub>O<sub>3</sub>)/carbon black electrodes for electrochemical capacitors, *Mater. Lett.* **2012**, 85, 40-43, DOI 10.1016/j.matlet.2012.06.109.
- [36] Lee, K.; Deng, S.; Fan, H.; Mhaisalkar, S.; Tan, H.; Tok, E.; Loh, K.; Chin, W.; Sow, C.  $\alpha$ -Fe<sub>2</sub>O<sub>3</sub> nanotubes-reduced graphene oxide composites as synergistic electrochemical capacitor materials, *Nanoscale*. **2012**, 4, 2958-2961, DOI 10.1039/c2nr11902a.
- [37] Yang, S.; Song, X.; Zhang, P.; Gao, L. Heating-rate-induced porous  $\alpha$ -Fe<sub>2</sub>O<sub>3</sub> with controllable pore size and crystallinity grown on graphene for supercapacitors, *ACS Appl. Mater. Inter.* **2015**, 7, 75-79, DOI 10.1021/am507910f.
- [38] Wang, Z.; Ma, C.; Wang, H.; Liu, Z.; Hao, Z. Facilely synthesized Fe<sub>2</sub>O<sub>3</sub>-graphene

- nanocomposite as novel electrode materials for supercapacitors with high performance, *J. Alloy. Compd.* **2013**, 552, 486-491, DOI 10.1016/j.jallcom.2012.11.071.
- [39] Chen, H.; Wang, C.; Lu, S.  $\gamma$ -Fe<sub>2</sub>O<sub>3</sub>/graphene nanocomposites as a stable high performance anode material for neutral aqueous supercapacitors, *J. Mater. Chem. A* **2014**, 2, 16955-16962, DOI 10.1039/c4ta03574g.
- [40] Wang, D.; Li, Y.; Wang, Q.; Wang, T. Nanostructured Fe<sub>2</sub>O<sub>3</sub>-graphene composite as a novel electrode material for supercapacitors, *J. Solid State Electr.* **2011**, 16, 2095-2102, DOI 10.1007/s10008-011-1620-4.
- [41] Low, Q.; Ho, G. Facile structural tuning and compositing of iron oxide-graphene anode towards enhanced supacapacitive performance, *Nano Energy*. **2014**, 5, 28-35, DOI 10.1016/j.nanoen.2014.01.002.
- [42] Yang, S.; Song, X.; Zhang, P.; Sun, J.; Gao, L. Self-Assembled  $\alpha$ -Fe<sub>2</sub>O<sub>3</sub> mesocrystals/graphene nanohybrid for enhanced electrochemical capacitors, *Small* **2014**, 10, 2270-2279, DOI 10.1002/sml.201303922.
- [43] Wang, H.; Tang, C.; Wang, B.; Li, B.; Zhang, Q. Bifunctional transition metal hydroxysulfides: room-temperature sulfurization and their applications in Zn-Air batteries, *Adv. Mater.* **2017**, 29, 1702327, DOI 10.1002/adma.201702327.
- [44] Gu, T.; Wei, B. High-performance all-solid-state asymmetric stretchable supercapacitors based on wrinkled MnO<sub>2</sub>/CNT and Fe<sub>2</sub>O<sub>3</sub>/CNT macrofilms, *J. Mater. Chem. A* **2016** 4, 12289-12295, DOI 10.1039/c6ta04712b.
- [45] Li, F.; Chen, H.; Liu, X.; Zhu, S.; Jia, J.; Xu, C.; Dong, F.; Wen, Z.; Zhang, Y. Low-cost high-performance asymmetric supercapacitors based on Co<sub>2</sub>AlO<sub>4</sub>@MnO<sub>2</sub> nanosheets and Fe<sub>3</sub>O<sub>4</sub> nanoflakes, *J. Mater. Chem. A* **2016**, 4, 2096-2104, DOI 10.1039/c5ta09914e.
- [46] Jiang, H.; Niu, H.; Yang, X.; Sun, Z.; Li, F.; Wang, Q.; Qu, F. Flexible Fe<sub>2</sub>O<sub>3</sub> and V<sub>2</sub>O<sub>5</sub> nanofibers as binder-free electrodes for high-performance all-solid-state asymmetric

- 1  
2  
3       supercapacitors, *Chem. Eur. J.* **2018**, 24, 10683-10688, DOI 10.1002/chem.201800461.  
4  
5  
6 [47] Tang, X.; Jia, R.; Zhai, T.; Xia, H. Hierarchical Fe<sub>3</sub>O<sub>4</sub>@Fe<sub>2</sub>O<sub>3</sub> core-shell nanorod arrays  
7  
8       as high-performance anodes for asymmetric supercapacitors, *ACS Appl. Mater.*  
9  
10       *Interfaces* **2015**, 7, 27518-27525, DOI 10.1021/acsami.5b09766.  
11  
12 [48] Zhang, S.; Yin, B.; Wang, Z.; Peter, F. Super long-life all solid-state asymmetric  
13  
14       supercapacitor based on NiO nanosheets and  $\alpha$ -Fe<sub>2</sub>O<sub>3</sub> nanorods, *Chem. Eng. J.* **2016**,  
15  
16       306, 193-203, DOI 10.1016/j.cej.2016.07.057.  
17  
18  
19  
20  
21  
22  
23  
24  
25  
26  
27  
28  
29  
30  
31  
32  
33  
34  
35  
36  
37  
38  
39  
40  
41  
42  
43  
44  
45  
46  
47  
48  
49  
50  
51  
52  
53  
54  
55  
56  
57  
58  
59  
60

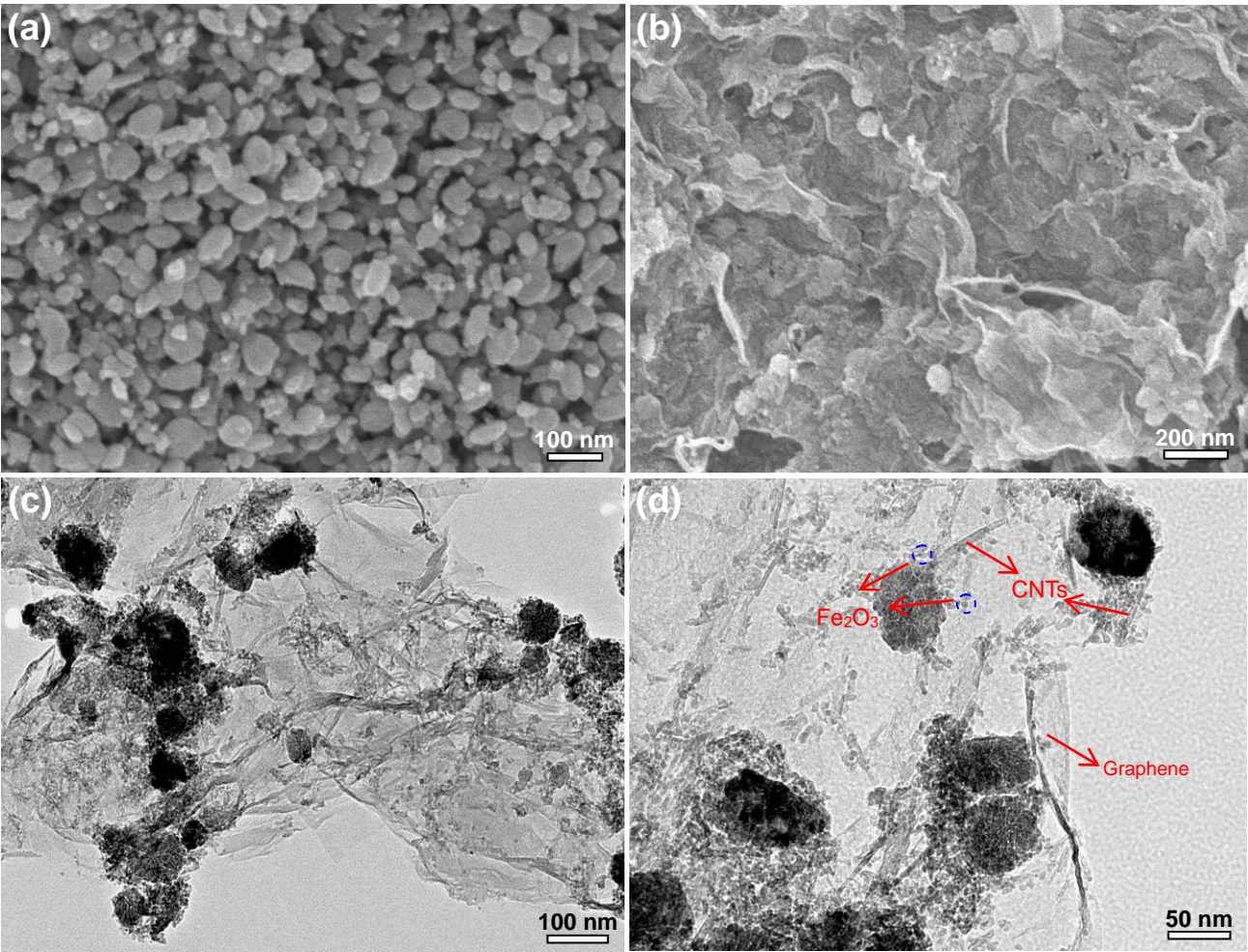


**Fig. 1.** SEM images of (a) pure Fe<sub>2</sub>O<sub>3</sub>, (b) Fe<sub>2</sub>O<sub>3</sub>/GNs/CNTs. (c, d) TEM images of Fe<sub>2</sub>O<sub>3</sub>/GNs/CNTs composite.

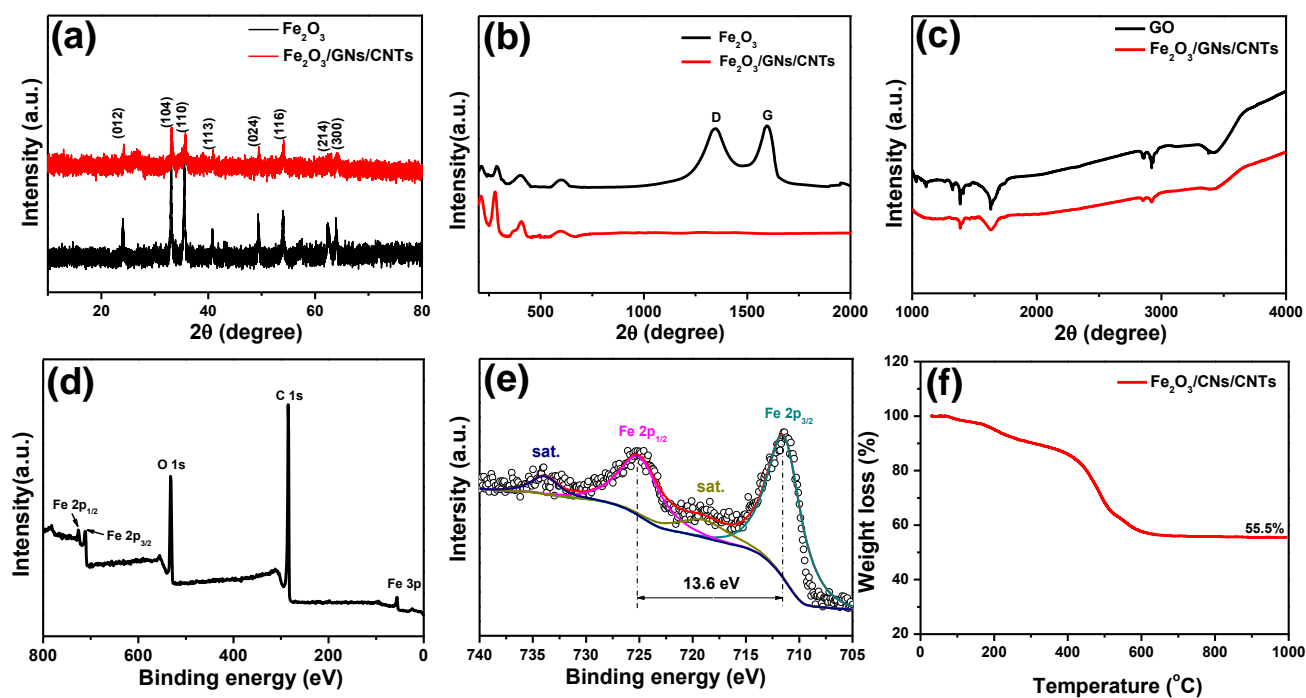


**Fig. 2.** (a) XRD patterns of pure  $\text{Fe}_2\text{O}_3$  and  $\text{Fe}_2\text{O}_3/\text{GNs}/\text{CNTs}$  composite. (b) Raman spectra of pure  $\text{Fe}_2\text{O}_3$  and  $\text{Fe}_2\text{O}_3/\text{GNs}/\text{CNTs}$  composite. (c) FT-IR spectrums of GO and  $\text{Fe}_2\text{O}_3/\text{GNs}/\text{CNTs}$  composite. (d) XPS survey spectrum of the  $\text{Fe}_2\text{O}_3/\text{GNs}/\text{CNTs}$  composite. (e) High-resolution Fe 2p spectra of the  $\text{Fe}_2\text{O}_3/\text{GNs}/\text{CNTs}$  composite. (f) TGA curve of the  $\text{Fe}_2\text{O}_3/\text{GNs}/\text{CNTs}$  composite.

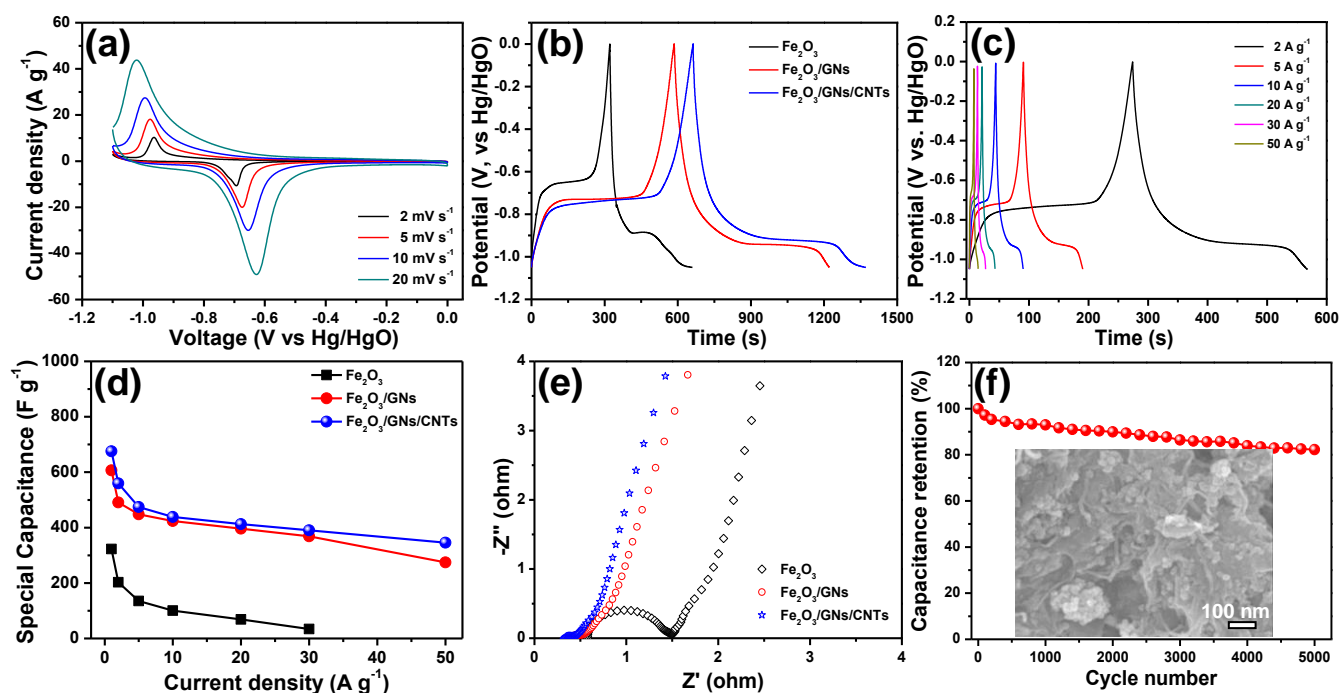


**Fig. 3.** (a) CV curves of  $\text{Fe}_2\text{O}_3/\text{GNs}/\text{CNTs}$  at different scan rates. (b) Galvanostatic discharge curves of  $\text{Fe}_2\text{O}_3$ ,  $\text{GNs}/\text{Fe}_2\text{O}_3$  and  $\text{Fe}_2\text{O}_3/\text{GNs}/\text{CNTs}$  at a current density of  $1 \text{ A g}^{-1}$ . (c) Galvanostatic discharge curves of  $\text{Fe}_2\text{O}_3/\text{GNs}/\text{CNTs}$  at different current densities. (d) Specific capacity of  $\text{Fe}_2\text{O}_3$ ,  $\text{Fe}_2\text{O}_3/\text{GNs}$  and  $\text{Fe}_2\text{O}_3/\text{GNs}/\text{CNTs}$  at different current densities. (e) Nyquist plots of the  $\text{Fe}_2\text{O}_3$ ,  $\text{Fe}_2\text{O}_3/\text{GNs}$  and  $\text{Fe}_2\text{O}_3/\text{GNs}/\text{CNTs}$  electrodes. (f) Cycling performance of the  $\text{Fe}_2\text{O}_3/\text{GNs}/\text{CNTs}$  electrode. The inset illustrates SEM image of  $\text{Fe}_2\text{O}_3/\text{GNs}/\text{CNTs}$  after 5000 cycle tests.

**Table 1** Summary of electrochemical performance for Fe<sub>2</sub>O<sub>3</sub>-based electrode materials.

Material	C (F g <sup>-1</sup> )	Electrolyte	Ref.
Fe <sub>2</sub> O <sub>3</sub>	100.6 (1mA cm <sup>-2</sup> )	3 M LiCl	[9]
Fe <sub>2</sub> O <sub>3</sub>	908.0 (2 A g <sup>-1</sup> )	2 M KOH	[31]
Fe <sub>2</sub> O <sub>3</sub>	558.7 F g <sup>-1</sup> (1 A g <sup>-1</sup> )	2 M KOH	[32]
Fe <sub>2</sub> O <sub>3</sub>	257.8 (1.4 A g <sup>-1</sup> )	5 M LiCl	[33]
Fe <sub>2</sub> O <sub>3</sub>	116.3 (5 mV s <sup>-1</sup> )	1 M Li <sub>2</sub> SO <sub>4</sub>	[34]
Fe <sub>2</sub> O <sub>3</sub> /graphene	618.0 (0.5 A g <sup>-1</sup> )	1 M KOH	[27]
Fe <sub>2</sub> O <sub>3</sub> /graphene	908.0 (2 A g <sup>-1</sup> )	1 M KOH	[28]
Fe <sub>2</sub> O <sub>3</sub> /carbon black	40.1 (10 mV s <sup>-1</sup> )	2 M KCl	[35]
Fe <sub>2</sub> O <sub>3</sub> /graphene	215.0 (2.5 mV s <sup>-1</sup> )	1 M Na <sub>2</sub> SO <sub>4</sub>	[36]
Fe <sub>2</sub> O <sub>3</sub> /graphene	343.7 (3 A g <sup>-1</sup> )	1 M Na <sub>2</sub> SO <sub>4</sub>	[37]
Fe <sub>2</sub> O <sub>3</sub> /graphene	226.0 (1 A g <sup>-1</sup> )	1 M Na <sub>2</sub> SO <sub>4</sub>	[38]
Fe <sub>2</sub> O <sub>3</sub> /graphene	224.0(25 mV s <sup>-1</sup> )	1 M Na <sub>2</sub> SO <sub>3</sub>	[39]
Fe <sub>2</sub> O <sub>3</sub> /graphene	151.8 (1 A g <sup>-1</sup> )	2 M KOH	[40]
Fe <sub>2</sub> O <sub>3</sub> /graphene	504 (2 mA cm <sup>-2</sup> )	1 M Na <sub>2</sub> SO <sub>4</sub>	[41]
Fe <sub>2</sub> O <sub>3</sub> /graphene	306.9 (3 A g <sup>-1</sup> )	1 M Na <sub>2</sub> SO <sub>4</sub>	[42]
Fe <sub>2</sub> O <sub>3</sub> /GNs/CNTs	<b>675.7 (1 A g<sup>-1</sup>)</b>	<b>6 M KOH</b>	<b>This work</b>



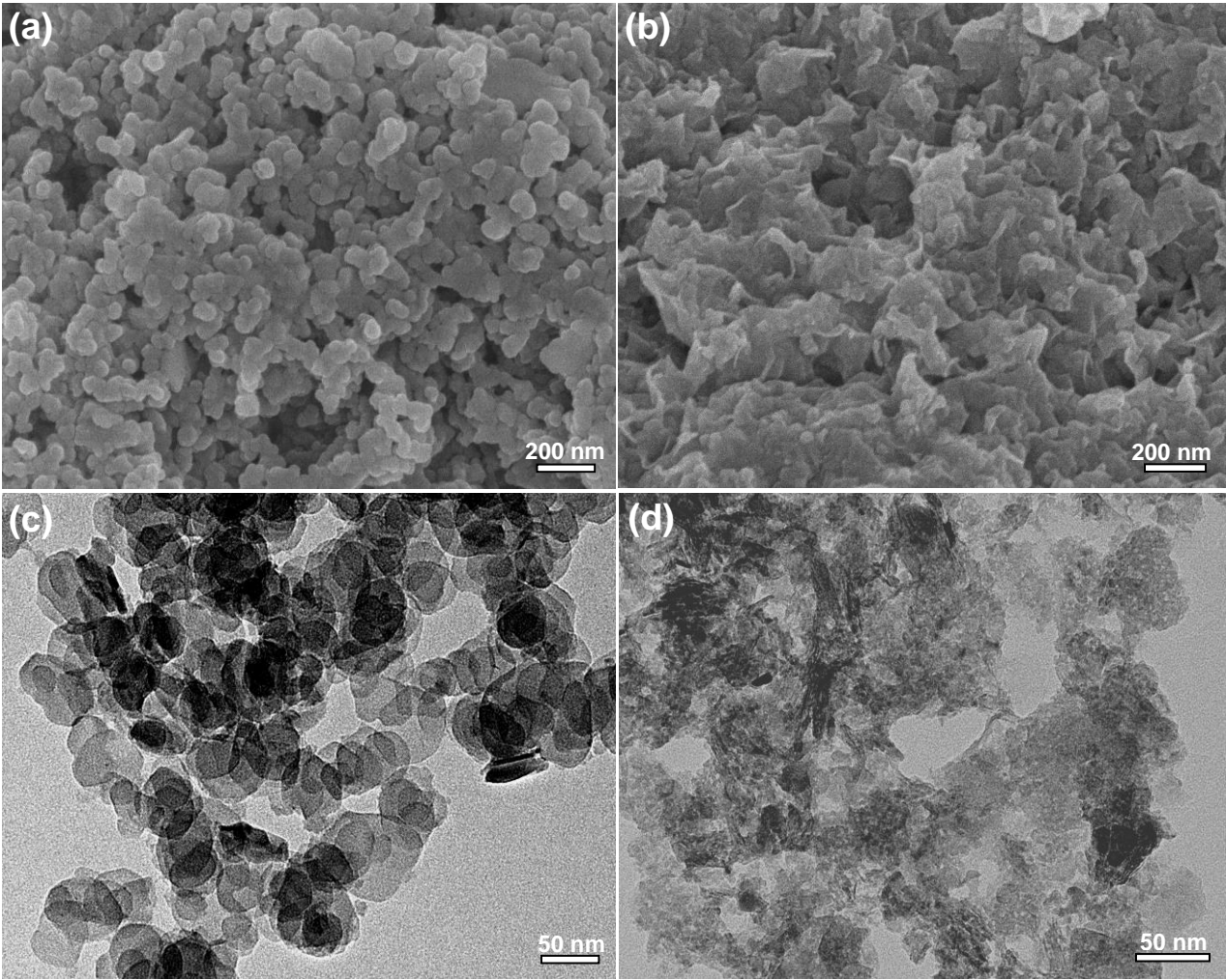


**Fig. 4.** (a) SEM image of LDH. (b) SEM image of SLDH. (c) TEM image of LDH. (d) TEM image of SLDH.



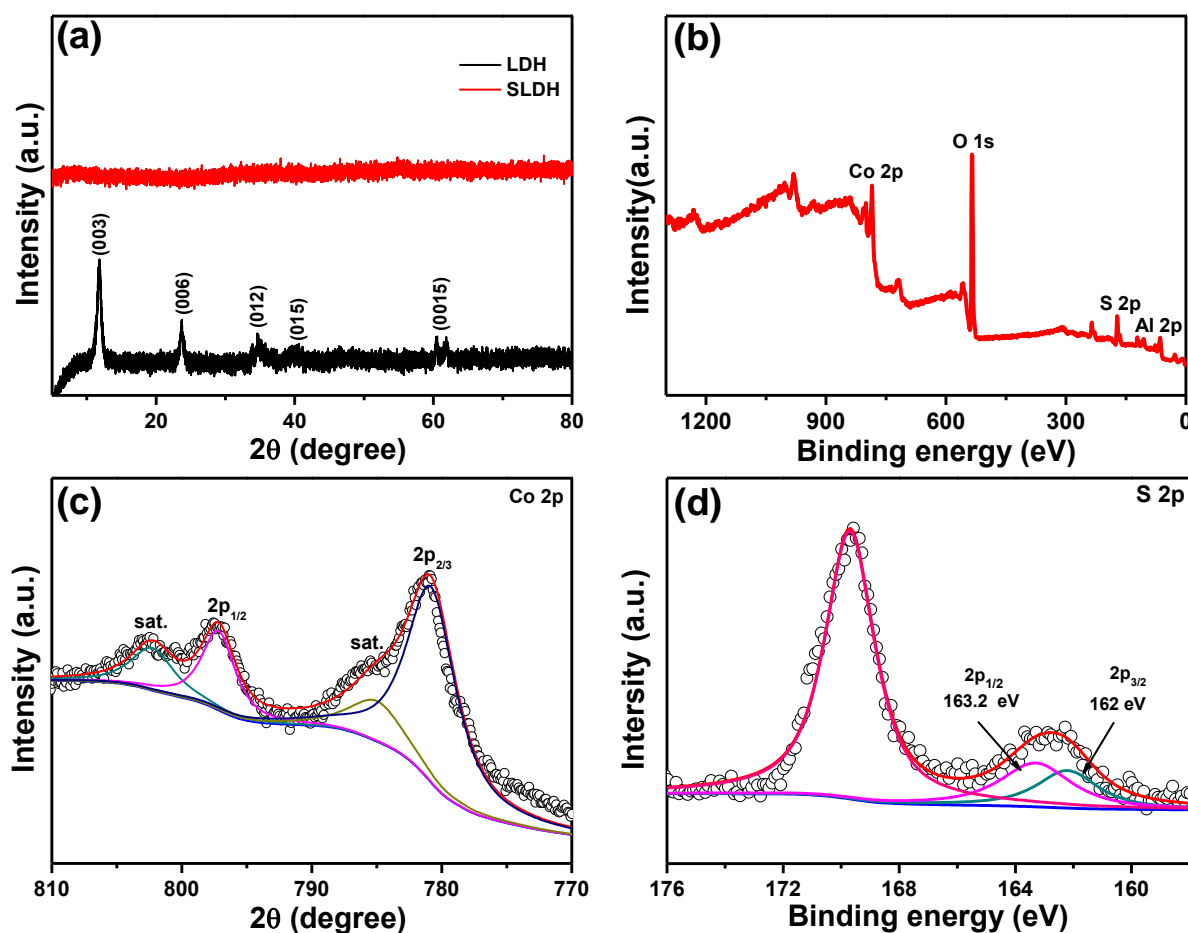


**Fig. 5.** (a) XRD patterns of the LDH and SLDH samples. (b) XPS survey spectrum of the SLDH samples. (c) High-resolution Co 2p spectra of the SLDH samples. (d) High-resolution S 2p spectra of the SLDH samples.

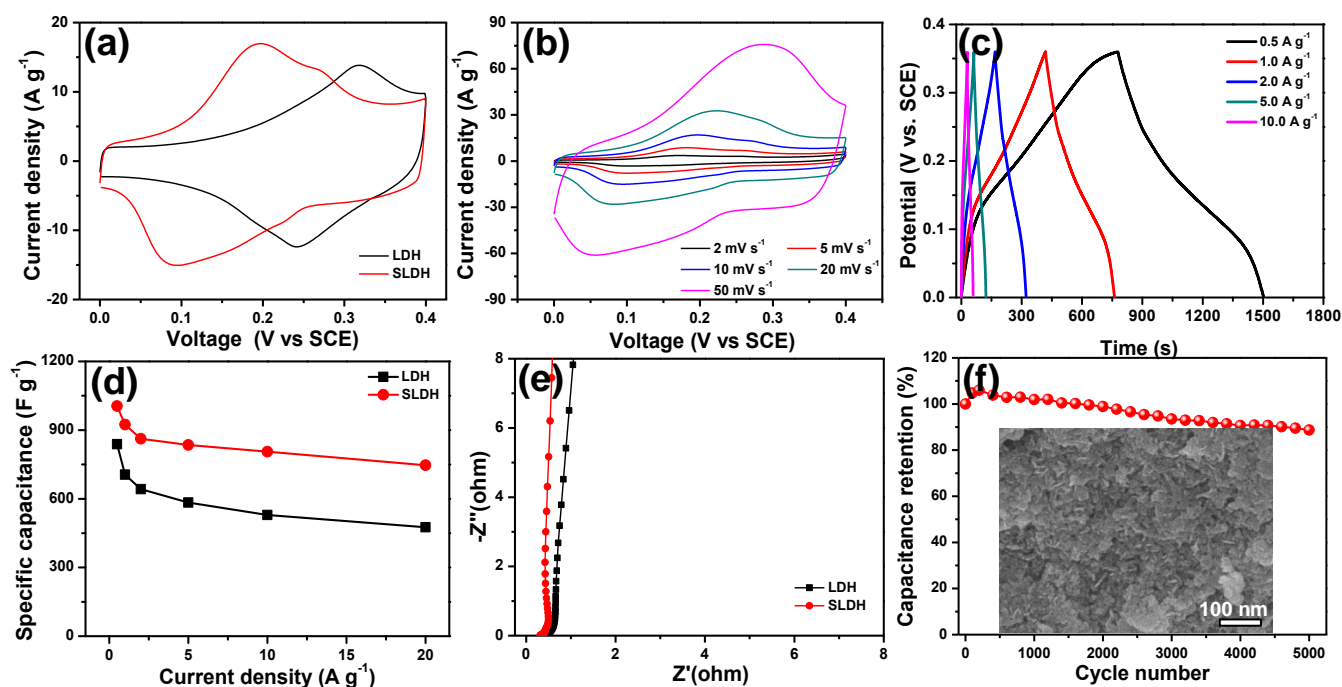


**Fig. 6.** (a) CV curves of LDH and SLDH at the scan rate of 10 mV s<sup>-1</sup>. (b) CV curves of S-LDH at different scan rates. (c) Galvanostatic charge-discharge profiles of SLDH at different current densities. (d) Specific capacity of LDH and SLDH at different current densities. (e) Nyquist plots of the LDH and SLDH electrodes. (f) Cycling performance of the SLDH electrode. The inset illustrates SEM image of SLDH after 5000 cycle tests.

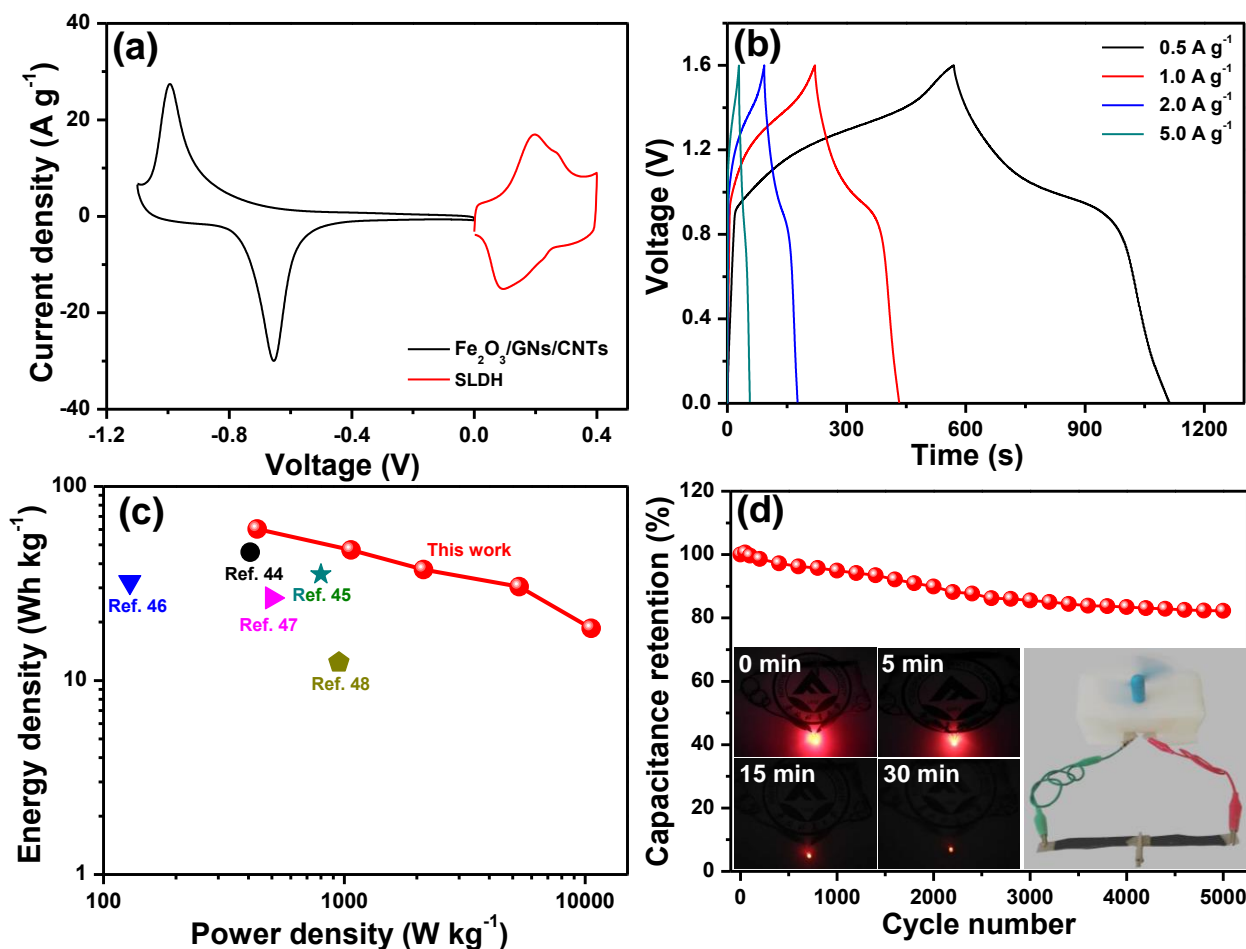
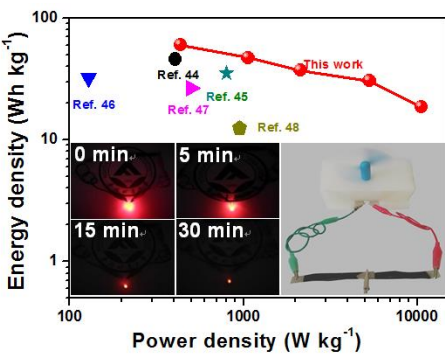


**Fig. 7.** (a) Comparative CV curves of  $\text{Fe}_2\text{O}_3/\text{GNs}/\text{CNTs}$  and SLDH electrodes performed in a three-electrode cell in 6 M KOH aqueous solution at a scan rate of  $10 \text{ mV s}^{-1}$ . (b) CV curves of the  $\text{Fe}_2\text{O}_3/\text{GNs}/\text{CNTs}$ //SLDH asymmetric supercapacitor at different scan rates with PVA/KOH polymer electrolyte. (c) Ragone plot of the  $\text{Fe}_2\text{O}_3/\text{GNs}/\text{CNTs}$ //SLDH all-solid-state asymmetric supercapacitor and the values reported previously. (d) Cycling performance of the  $\text{Fe}_2\text{O}_3/\text{GNs}/\text{CNTs}$ //SLDH all-solid-state asymmetric supercapacitor.

For Table of Contents Use Only



Synopsis

A facile and sustainable way was developed to prepare Fe<sub>2</sub>O<sub>3</sub>/graphene/CNTs composite, which has potential for supercapacitors.